

**Numerical Simulations of Evaporating Sprays in High
Pressure and Temperature Operating Conditions
(Engine Combustion Network [ECN])**

by Luis Bravo and Chol-Bum Kweon

ARL-TR-6938

May 2014

NOTICES

Disclaimers

The findings in this report are not to be construed as an official Department of the Army position unless so designated by other authorized documents.

Citation of manufacturer's or trade names does not constitute an official endorsement or approval of the use thereof.

Destroy this report when it is no longer needed. Do not return it to the originator.

Army Research Laboratory

Aberdeen Proving Ground, MD 21005-5069

ARL-TR-6938**May 2014**

Numerical Simulations of Evaporating Sprays in High Pressure and Temperature Operating Conditions (Engine Combustion Network [ECN])

Luis Bravo and Chol-Bum Kweon
Vehicle Technology Directorate, ARL

REPORT DOCUMENTATION PAGE				Form Approved OMB No. 0704-0188	
Public reporting burden for this collection of information is estimated to average 1 hour per response, including the time for reviewing instructions, searching existing data sources, gathering and maintaining the data needed, and completing and reviewing the collection information. Send comments regarding this burden estimate or any other aspect of this collection of information, including suggestions for reducing the burden, to Department of Defense, Washington Headquarters Services, Directorate for Information Operations and Reports (0704-0188), 1215 Jefferson Davis Highway, Suite 1204, Arlington, VA 22202-4302. Respondents should be aware that notwithstanding any other provision of law, no person shall be subject to any penalty for failing to comply with a collection of information if it does not display a currently valid OMB control number. PLEASE DO NOT RETURN YOUR FORM TO THE ABOVE ADDRESS.					
1. REPORT DATE (DD-MM-YYYY) May 2014		2. REPORT TYPE Final		3. DATES COVERED (From - To) September 2013–December 2013	
4. TITLE AND SUBTITLE Numerical Simulations of Evaporating Sprays in High Pressure and Temperature Operating Conditions (Engine Combustion Network [ECN])				5a. CONTRACT NUMBER	
				5b. GRANT NUMBER	
				5c. PROGRAM ELEMENT NUMBER	
6. AUTHOR(S) Luis G. Bravo and Chol-Bum Kweon				5d. PROJECT NUMBER	
				5e. TASK NUMBER	
				5f. WORK UNIT NUMBER	
7. PERFORMING ORGANIZATION NAME(S) AND ADDRESS(ES) U.S. Army Research Laboratory ATTN: RDRL-VTP Aberdeen Proving Ground, MD 21005-5069				8. PERFORMING ORGANIZATION REPORT NUMBER ARL-TR-6938	
9. SPONSORING/MONITORING AGENCY NAME(S) AND ADDRESS(ES)				10. SPONSOR/MONITOR'S ACRONYM(S)	
				11. SPONSOR/MONITOR'S REPORT NUMBER(S)	
12. DISTRIBUTION/AVAILABILITY STATEMENT Approved for public release; distribution is unlimited.					
13. SUPPLEMENTARY NOTES					
14. ABSTRACT A series of evaporating n-dodecane spray numerical studies are conducted under typical diesel engine operating conditions. The objective of this report is to demonstrate the modeling capability of a recently adopted 3D-Computational Fluid Dynamics (CFD) solver and provide expertise in simulations of complex multiphase flows. Two benchmark cases were selected based on the Engine Combustion Network (ECN) collaborators from Sandia National Laboratories (U.S.), and CMT-Motores (Spain). The simulations results were able to accurately predict the results including the standardized "Spray A" single condition at rail pressure 1500 bar and ambient conditions of 900 K and 60 bar (Sandia), and the more challenging conditions including variations in rail pressure 500–1500 bar and fuel temperatures 331–377 K (CMT-Motores). The results show the ability of the simulations to be predictive at various challenging conditions. Similar capabilities are presently available at the U.S. Army Research Laboratory's (ARL's) Spray Combustion Research Laboratory and hence this study provides the benchmarking needed to enable next-phase simulations of our in-house JP-8 data.					
15. SUBJECT TERMS CFD, spray, turbulence, engines, diesel, JP-8					
16. SECURITY CLASSIFICATION OF:			17. LIMITATION OF ABSTRACT UU	18. NUMBER OF PAGES 34	19a. NAME OF RESPONSIBLE PERSON Luis G. Bravo
a. REPORT Unclassified	b. ABSTRACT Unclassified	c. THIS PAGE Unclassified			19b. TELEPHONE NUMBER (Include area code) 410-278-9018

Contents

List of Figures	iv
List of Tables	v
1. Summary	1
2. Introduction	2
3. Numerical Method	4
3.1 Governing Equations	4
3.2 Time Advancement	6
3.3 Spray Modeling	7
4. Results and Discussions	8
4.1 ECN, Sandia Spray A Conditions	9
4.2 ECN, CMT Spray A conditions (Fuel-Temperature Effects).....	15
5. Conclusions	21
6. References	23
List of Symbols, Abbreviations, and Acronyms	25
Distribution List	26

List of Figures

Figure 1. Sandia National Laboratories (a) CVP facility, (b) schematic of CVP setup.	9
Figure 2. Spray A convergence properties at various embed scales corresponding to $dx = 2, 1, 0.5, 0.25, 0.125, 0.0625$ mm: (a) liquid penetration vs. time, (b) vapor penetration vs. time, (c) peak liquid penetration vs. embed scale.	11
Figure 3. Multi-institutional experimental comparison of Spray A penetration profiles: (a) liquid penetration, (b) vapor penetration. Embed scale of three, $dx = 0.25$ mm.	12
Figure 4. Mie scattering imaging sequence at IFP and Sandia and comparison to ARL's CFD model for Spray A conditions.	13
Figure 5. Spray A visualization (a) contour of velocity and (b) contours of fuel-mass fraction. Note that spray is surrounded by the vapor line at $Y_f = 0.01$	14
Figure 6. CMT-Motores, Universidad Politecnica de Valencia: (a) CPF facility, (b) schematic of CPF setup.	15
Figure 7. Rate of injection (ROI) profiles for CMT cases A1–A3 using the CMT virtual injection generator.	17
Figure 8. Spray penetration profiles at $P_\infty = 60 \text{ bar}$; $T_\infty = 900K$, $\rho_\infty = 22.8 \text{ kg/m}^3$ ambient conditions with fixed $P_{inj} = 1500 \text{ bar}$ while varying fuel temperature $T_f = 341K, 369K, 391K$	18
Figure 9. Spray injection and penetration profiles at $P_\infty = 60 \text{ bar}$; $T_\infty = 820K$, $\rho_\infty = 22.8 \text{ kg/m}^3$ ambient conditions and fuel temperature $T_f = 331 \text{ K}$. (a) ROI profiles used for cases b–d, (b) liquid/vapor profiles at $P_{inj} = 500 \text{ bar}$, (c) liquid/vapor profiles at $P_{inj} = 1000 \text{ bar}$, liquid/vapor profiles at $P_{inj} = 1500 \text{ bar}$	19
Figure 10. Spray injection and penetration profiles at $P_\infty = 60 \text{ bar}$; $T_\infty = 820K$, $\rho_\infty = 22.8 \text{ kg/m}^3$ ambient conditions and fuel temperature $T_f = 377 \text{ K}$. (a) ROI profiles used for cases b–d, (b) liquid/vapor profiles at $P_{inj} = 500 \text{ bar}$, (c) liquid/vapor profiles at $P_{inj} = 1000 \text{ bar}$, liquid/vapor profiles at $P_{inj} = 1500 \text{ bar}$	20
Figure 11. Effect of T_f variation over liquid penetration length for different injection pressures (at $\rho_\infty = 22.8 \text{ kg/m}^3$) for (a) $T_f = 331 \text{ K}$, (b) $T_f = 377 \text{ K}$	21

List of Tables

Table 1. Injector and spray conditions (Spray A).	10
Table 2. CFD embed scale and number of injected particles.	10
Table 3. CMT vessel conditions.	16
Table 4. Coolant and injector sac fuel temperature.	16
Table 5. CONVERGE test cases.....	17

INTENTIONALLY LEFT BLANK.

1. Summary

The U.S. Army Research Laboratory (ARL), Vehicle Technology Directorate (VTD), has recently commissioned a state-of-the-art Constant Pressure Flow (CPF) combustion vessel facility enabling fundamental spray and combustion studies of critical importance to the mission. The facility operates using several fuels including diesel, JP-8, Hydrotreated Renewable Jet (HRJ), and Iso-Paraffinic Kerosene (IPK) and can carry out experiments at maximum temperature and pressure conditions of 1000 K and 150 bar while maintaining steady conditions. Common rail and Hydraulically-actuated Electronically-controlled Unit Injector (HEUI) injectors provide liquid fuel sprays at diesel operating conditions typically from 200 to 1800 bar. Spray measurements are obtained using advanced optical diagnostics such as Mie scattering, shadowgraph, and schlieren imaging. Hence the facility provides a critical database promoting technology development for unmanned aerial vehicle (UAV) systems (i.e., Shadow, Hunter, and Gray Eagle) and improvements in several existing power focus areas (i.e., compact components, increased power density and fuel efficiency).

In response to this, a multiphase flow solver CONVERGE, developed by Convergent Science, Inc. (CSI), has been adopted to enable 3D-Computational Fluid Dynamics (CFD) spray simulations at diesel engine operating conditions. The solver is based on the classical Eulerian-Lagrangian formulation and blob-injection wave models to treat the spray as two interacting fluids. Over the years, conducting spray simulations have demonstrated to be of paramount importance in the research process. Some important features include its suitability in conducting extensive cost-effective parametric and optimization studies, its ability to provide a complete history of multidimensional resolved information for every variable, and its ability to artificially separate specific subprocesses that would inherently interact in an experiment. Although CFD-based tools have steadily improved and continue to provide higher quality models, a vast number of experiments will remain necessary to guide and control simulation results, to validate and calibrate existing models, and in driving the development of next-generation models. Consequently, a much better analysis for the interpretation of complex results will be available, if both numerical and experimental studies are conducted in parallel.

Historically, the CFD community has benefited from spray measurements that have driven the model development process. Validation studies will reveal the suitability of the modeling assumptions (physical models), stability of the spatio-temporal numerical technique (numerical methods), and calibration of model parameters (turbulence, breakup, combustion constants) that is required to carefully benchmark a simulation. In this report, several studies are conducted at diesel engine operating conditions to demonstrate the modeling capability of CONVERGE. The databases used are part of the Engine Combustion Network (ECN) library. The results demonstrate the suitability of the models used, physical assumptions, and boundary conditions.

Spray simulations are in good agreements with experiments, providing confidence in modeling procedure, and enabling further studies.

2. Introduction

In many combustion systems, fuel atomization and the spray breakup process play an important role in determining combustion characteristics and emissions formation. Due to the ever rising need for better fuel efficiency and lower emissions, the development of a fundamental understanding of its process is essential and remains a challenging task. In the U.S. military air and ground vehicle applications, the characterization of engines operating with JP-8 fuels is critical in developing new vehicle propulsion technologies and enhancing existing compact fuel-to-electric power systems. Hence, the control of spray characteristics will remain of critical priority in enabling the Army mission of driving new technologies, optimizing engine performance, while facilitating fuel logistics operations.

In modern engines, the spray process begins with a high-pressure liquid fuel injected into a vessel at high temperature and pressure conditions. A liquid core-jet is formed; its penetration length is influenced by several factors including nozzle orifice, internal nozzle conditions, fuel-air turbulent mixing, external ambient conditions, and physical properties. The interaction of the fuel jet with its surroundings promotes liquid atomization into fine droplets as a result of aerodynamic instabilities and surface tension forces. The continuation of the process leads to further breakup, droplet-droplet interactions, droplet-wall interactions, and evaporation. If critical conditions are present, the fuel may self-ignite leading to a combustion event and generating a specific amount of power output. Research studies providing access to spray measurements will remain critical in enabling new understanding of the spray process.

Remarkable progress has been made characterizing the spray behavior in both experimental and numerical studies. Experimentally, Siebers (1) has studied the behavior of evaporating diesel sprays and has reported the effects of several operating condition on the liquid and vapor spray penetrations, kinematics, and mixture fraction. It was reported that liquid length decreases linearly with injector orifice diameter, temperature, and increases with fuel volatility or temperature, and that it is weakly dependent on injector pressure. In a cross-institutional study, Picket et al. (2) has presented the operational details of lab instrumentation, and experimental conditions across several platforms in an effort to enhance the fidelity of spray diagnostics. Payri et al. (3) has studied the fuel-temperature effect in nonreacting and reacting diesel sprays using a novel injector, and imaging diagnostics for liquid phase penetration, light-off length, and ignition delay measurements. Payri et al. (3) reported a clear influence of the injector body temperature, real fuel temperature, on nonreactive and in a lesser degree to reacting sprays. More recent studies have focused on resolving the structure of the spray's liquid core by use of x-ray techniques and medical imaging (4–6). Wang et al. (4) used x-ray phase contrast imaging to

study the near nozzle atomization process of air assisted water sprays. Key observations were made about the atomization process at high-We numbers, such as jet narrowing, spray breakup, and the tracking of the mass volume fraction. Coletti et al. (6) has introduced x-ray computed tomography (CT) technique to provide detailed information of the spray dense region. Medical software is used for imaging to reconstruct a three-dimensional time-averaged distribution of liquid mass fraction from the intact core to the dilute spray region. This progress has provided new insights into the spray including the near nozzle region improving our understanding and driving the generation of enhanced spray models.

Over the years, 3D-CFD multiphase solvers have been developed largely based on Lagrangian particle tracking methods coupled with wave type spray models and appropriate source terms. In a study of spray induced turbulence, Banerjee and Rutland (7) has used a traditional code (KIVA) with a selection of modern turbulence models on various grids. The study reported on the resolution study conducted with large-eddy simulation (LES) methods leading to CFD mesh criteria based on the breakdown of large flow coherent structures. Also using the KIVA solver, Bharadwaj et al. (8) presented LES results for a particle laden gas jet and nonevaporative diesel sprays obtaining good agreements with Argonne National Laboratory (ANL) x-ray measured data. The objective was to demonstrate the capability of LES in predicting two-phase interaction while modeling of the subgrid scale droplet effects on turbulent kinetic energy. More recently, Senecal et al. (9) has demonstrated grid-convergent properties using the state-of-the-art CONVERGE solver and provided guidelines to benchmark against ECN spray measurements. In an effort to capture injector cavitation and turbulence effects on spray atomization models, Som et al. (10) introduced the Kelvin-Helmholtz-Aerodynamics Cavitation Turbulence (KH-ACT) model and demonstrated its fidelity through validation across several spray configurations. It was observed that the inclusion of cavitation and turbulence enhances primary atomization decreasing spray droplet sizes, reducing penetration lengths, and increasing radial dispersion. As a consequence, the model provides better agreements with measurements of non-evaporating and evaporating sprays. In 2013, Senecal et al. (11) extended his previous spray study to transient LES methods, recalibration of spray parameters, and the effect of cycle to cycle averaging on spray diagnostics. A similar study was conducted by Xue et al. (12) focusing on grid-convergence studies with comparison to ECN data denoted as Spray-A and Spray-H and hence developing grid criteria. These studies have enabled practical engineering simulations leading to enhanced understanding and advancements in technology developments and research process.

In this report, several 3D-CFD validation studies are conducted to demonstrate the modeling capability of the CONVERGE solver. Two databases were selected providing a wide range of operating condition relevant to diesel engine configurations. The databases used are from the ECN and are representative of present research studies providing a synergistic approach to research. The report is organized in the following manner. A brief literature review on experimental and numerical spray studies has been presented with a focus on recent trends. A description of the governing equations, time advancement method, turbulence, and spray model

is presented to establish the accuracy of the solver and its numerical methodology. The results are then discussed in two sections where comparisons are made to the ECN measurements at various conditions. The ECN databases used correspond to the classical Spray A conditions from Sandia National Laboratories, and CMT-Motores study of fuel-temperature effects on spray penetration behavior. Conclusions and future efforts are discussed.

3. Numerical Method

The CONVERGE 3D-CFD solver, developed by CSI, has been adopted in this study to perform detailed spray simulations at realistic engine operating conditions. CONVERGE is a compressible Navier Stokes solver, it is based on a first order predictor-corrector (Pressure Implicit with Splitting of Operator [PISO]) time integration scheme, and a choice of second or higher order finite volume schemes for spatial discretization. It features a nonstaggered, collocated, computation grid framework using a Rhie-Chow interpolation technique to avoid spurious oscillations. An efficient geometric multigrid treatment is used to solve the pressure equation, and a parallel computing implementation is based on implementations of either OpenMP or Message Passing Interface (MPI) protocols. It provides the option of increasing resolution locally through static fixed-grid embedding and dynamically through Adaptive Mesh Refinement activated through user specified criteria. Additionally, it uses state-of-the-art Eulerian-Lagrangian spray models, and a parallel detailed chemistry solver for combustion that can be fully coupled with CHEMKIN databases. CONVERGE also provides a choice between a number of modeling options for the treatment of turbulence, including direct numerical simulation (DNS), LES, and Reynolds-averaged Navier-Stokes (RANS).

3.1 Governing Equations

In this study, the gas phase is described using the Favre-averaged Navier-Stokes Equations, and the RNG $k - \epsilon$ model for low-resolution turbulence studies has been adopted. The compressible system of transport equations for mass, momentum, energy, and species transport are presented here in a RANS framework.

Conservation of Mass:

$$\frac{\partial \bar{\rho}}{\partial t} + \frac{\partial \bar{\rho} \tilde{u}_j}{\partial x_j} = 0 \quad (1)$$

Conservation of Momentum:

$$\frac{\partial \bar{\rho} \tilde{u}_i}{\partial t} + \frac{\partial \bar{\rho} \tilde{u}_i \tilde{u}_j}{\partial x_j} = \frac{\partial \bar{P}}{\partial x_i} + \frac{\partial}{\partial x_i} \left[\mu \left(\frac{\partial \tilde{u}_j}{\partial x_i} + \frac{\partial \tilde{u}_i}{\partial x_j} \right) - \frac{2}{3} \mu \frac{\partial \tilde{u}_k}{\partial x_k} \delta_{ij} \right] + \frac{\partial}{\partial x_i} (-\bar{\rho} \tilde{u}_i' \tilde{u}_j') \quad (2)$$

The last term is denoted as the Reynolds stresses of the system, $\tau_{ij} = -\bar{\rho} \widetilde{u'_i u'_j}$. It needs to be modeled to provide mathematical closure and to account for turbulence effects. Turbulent viscosity formulation in RANS typically require the modeled Reynolds stress for the Standard $k - \epsilon$ and RNG to be represented as,

$$\tau_{ij} = \bar{\rho} \widetilde{u'_i u'_j} = 2\mu_t S_{ij} - \frac{2}{3} \delta_{ij} \left(\rho k + \mu_t \frac{\partial \widetilde{u'_i}}{\partial x_i} \right) \quad (3)$$

Hence, turbulent viscosity is defined as $\mu_t = C_\mu \rho (k^2/\epsilon)$, where k and ϵ are calculated classically by transporting two representative equations. Additionally, there is a model constant that typically carries the value of $C_\mu = 0.09$, and S_{ij} represents the mean strain rate tensor. The transport equations for the k and ϵ RANS model are given in order as,

$$\frac{\partial \rho k}{\partial t} + \frac{\partial \rho u_i k}{\partial x_i} = \tau_{ij} \frac{\partial u_i}{\partial x_j} + \frac{\partial}{\partial x_j} \left(\frac{\mu}{\text{Pr}_k} \frac{\partial k}{\partial x_j} \right) - \rho \epsilon + S_s \quad (4)$$

and,

$$\frac{\partial \rho \epsilon}{\partial t} + \frac{\partial (\rho u_i \epsilon)}{\partial x_i} = \frac{\partial}{\partial x_j} \left(\frac{\mu}{\text{Pr}_\epsilon} \frac{\partial \epsilon}{\partial x_j} \right) - C_{\epsilon 3} \rho \epsilon \frac{\partial u_i}{\partial x_i} + \left(C_{\epsilon 3} \frac{\partial u_i}{\partial x_j} \tau_{ij} - C_{\epsilon 2} \rho \epsilon + C_s S_s \right) \frac{\epsilon}{k} - \rho R \quad (5)$$

where the definition of R will vary depending on the choice of RANS turbulence model. It is defined as $R = 0$ for the Standard $k - \epsilon$ model and $R = C_\mu \eta^3 (1 - \eta/\eta_0) \epsilon^2 / (1 - \beta \eta^3) k$ for RNG $k - \epsilon$ model.

Note that the source terms, S_s , are included due to the Lagrangian-Eularian formulation and are important in describing the particle interaction with its surrounding. It is defined as,

$$S_s = \frac{\sum_p N_p (F'_{drag,i} u'_i)_p}{V} \quad (6)$$

where N_p is the number of drops in a parcel, V is the cell volume, u'_i is the gas phase turbulence fluctuation, and the summation is carried over all the parcels in each cell. Note that the drag force on each drop is defined as, $F'_{drag,i} = F_{drag,i} u'_i / u_i + u'_i - v_i$.

Heat and species mass transfer is treated using the compressible form of the energy equation and the species mass transfer equations. Note that the species transport solves for the mass fraction, Y_k , of all species in the specified system.

Conservation of Energy:

$$\frac{\partial \bar{\rho} \bar{e}}{\partial t} + \frac{\partial \bar{u}_j \bar{\rho} \bar{e}}{\partial x_j} = -\bar{P} \frac{\partial \bar{u}_j}{\partial x_j} + \sigma_{ij} \frac{\partial \bar{u}_i}{\partial x_j} + \frac{\partial}{\partial x_j} \left(K \frac{\partial \bar{T}}{\partial x_j} \right) + \frac{\partial}{\partial x_j} \left(\bar{\rho} \bar{D} \sum_k \bar{h}_m \frac{\partial \bar{Y}_k}{\partial x_j} \right) + S \quad (7)$$

Conservation of Species:

$$\frac{\partial \bar{\rho}_k}{\partial t} + \frac{\partial \bar{\rho}_k \bar{u}_j}{\partial x_j} = \frac{\partial}{\partial x_j} \left(\bar{\rho} \bar{D} \frac{\partial \bar{Y}_k}{\partial x_j} \right) + S_k \quad (8)$$

where e is the specific internal energy, K is the conductivity, h_k is the species enthalpy, D is the mass diffusion coefficient, and S_k the source term. For turbulent cases, the mass diffusion coefficient is calculated by $D_t = \nu_t / Sc_t$ in terms of turbulent viscosity and Schmidt numbers.

3.2 Time Advancement

Equations 1 and 2 are solved numerically using a classical predictor-corrector scheme in which the velocity field is first integrated using the Navier Stokes equation 2 and then corrected to enforce mass conservation (equation 1) using a modified pressure. This is achieved using the modified PISO algorithm first introduced by Issa et al. (13).

An illustration of the PISO predictor corrector sequence is presented below (note that H^* represents convection, diffusion, S accounts for implicit/explicit sources, and $*$ denotes the intermediate steps) for a one-time correction procedure,

Predictor step:

$$\frac{\rho^n u_i^*}{\partial t} - \frac{\rho^n u_i^n}{\partial t} = -\frac{\partial P^n}{\partial x_i} + H_i^* \quad (9)$$

Corrector steps:

$$\frac{\rho^* u_i^{**}}{\partial t} - \frac{\rho^n u_i^n}{\partial t} = -\frac{\partial P^*}{\partial x_i} + H_i^* \quad (10)$$

$$\frac{\partial^2}{\partial x_i \partial x_i} (P^* - P^n) - \frac{(P^* - P^n) \phi}{dt^2} = \left(\frac{\partial \rho^n u_i^*}{\partial x_i} - S \right) \frac{1}{dt} \quad (11)$$

Update step:

$$\frac{\rho^* u_i^{**}}{\partial t} - \frac{\rho^n u_i^*}{\partial t} = -\frac{\partial}{\partial x_i} (P^* - P^n) \quad (12)$$

where dt is the numerical integration time step. Once the pressure is solved, the velocity is recalculated according to the updated momentum equation.

3.3 Spray Modeling

Spray modeling is treated using the “blob” injection method of Reitz and Diwakar (14). Blobs of a characteristic size are injected following a statistical distribution into the computational domain. Primary and secondary breakups are subsequently simulated based on the Kelvin-Helmholts (KH) and Rayleigh-Taylor (RT) instability methods. Note that the breakup length is not determined a priori (breakup length concept) and is calculated as a part of the solution.

In the KH wave model, atomization is treated using stability analysis for liquid jets. The breakup of the injected blobs and resulting drops of radius r_o is calculated by assuming that the drop radius is proportional to the wavelength of the fastest growing unstable surface wave Λ_{KH} .

It is written as,

$$r = B_0 \Lambda_{KH} \quad (13)$$

where B_0 is a model constant. The droplet size, and its change of radius is in the following way,

$$\frac{dr_o}{dt} = -\frac{(r_o - r)}{\tau_{KH}} \quad (14)$$

where the breakup time constant, τ_{KH} , is calculated as,

$$\tau_{KH} = \frac{3.726 B_1 r_o}{\Lambda_{KH} \Omega_{KH}} \quad (15)$$

and the maximum growth rates Ω_{KH} and corresponding wavelengths Λ_{KH} have been simplified and defined as follows,

$$\Omega_{KH} \left(\frac{\rho_l a^3}{\sigma} \right) = \frac{0.34 + 0.38 W e_g^{1.5}}{(1+Z)(1+1.4T^{0.6})} \quad (16)$$

and,

$$\frac{\Lambda_{KH}}{a} = 9.02 \frac{(1+0.45Z^{0.5})(1+0.4T^{0.7})}{(1+0.87W e_g^{1.67})^{0.6}} \quad (17)$$

where,

$$Z = W e_l^{0.5} / Re_l, T = W e_g^{0.5}, W e_l = \rho_l U^2 a / \sigma, W e_g = \rho_g U^2 a / \sigma, \text{ and } Re_l = U a / \nu_l$$

The present RT mechanism formulation includes viscosity variations in the growth rate equation,

$$\omega_{RT} = -k_{RT}^2 \left(\frac{\mu_l + \mu_g}{\rho_l + \rho_g} \right) + \sqrt{k_{RT} \left(\frac{\rho_l - \rho_g}{\rho_l + \rho_g} \right) a - \frac{k_{RT}^3 \sigma}{\rho_l + \rho_g} + k_{RT}^4 \left(\frac{\mu_l + \mu_g}{\rho_l + \rho_g} \right)^2} \quad (18)$$

where k_{RT} is the wavenumber, μ_l is the liquid viscosity, μ_g is the gas viscosity, ρ_l is the liquid density, ρ_g the gas density, a is the deceleration of the drop, and σ is the liquid surface tension.

The wave number corresponding to the maximum growth rate $K_{RT} = 2\pi/\Lambda_{RT}$ is calculated through a bisection method with equation 18.

The value is updated to calculate the maximum growth rate Ω_{RT} . The predicted RT model drop size is then expressed as,

$$r_{RT} = C_{RT}\Lambda_{KH} \quad (19)$$

where C_{RT} is the model constant, and Λ_{KH} is the predicted RT wavelength. In summary the spray model constants used in this study are defined as: $B_0 = 0.6$, $B_1 = 12$, $C_{RT} = 0.1$, and $C_\tau = 1$.

Lastly, other spray processes that were modeled include droplet distortion and drag, droplet interactions in terms of collision and coalescence, turbulent dispersion, and evaporation. The two phases are coupled through the exchange of mass, momentum, and energy, represented in the appropriate source terms in the gas-phase equations. These models are described in detail in a recent review by Bravo and Kweon (15) and the reader is referred to that article.

4. Results and Discussions

Measurements selected from two databases were utilized to benchmark the CFD solution at various conditions. The databases can be readily extracted from the ECN Internet library operated by Sandia National Laboratories, Combustion Research Facility and available at <http://www.sandia.gov/ecn/>. The network provides access to detailed spray measurements conducted through the use of multi-institutional combustion vessels (CPF or Constant Volume Preburn [CVP] chambers) at various ambient gas compositions. Some of the ECN affiliates across several institutions that have conducted spray studies include: Sandia National Laboratories (U.S.), IFP (France), Universidad Politecnica de Valencia (Spain), Caterpillar (U.S.), and Eindhoven University of Technology (Netherlands). Their efforts have contributed to the breadth of the library by conducting reacting/non-reacting spray studies under several operating conditions, and fuels (i.e., gasoline, diesel)

Recently, several efforts have been reported attempting to standardize experimental configurations and procedures. An ideal configuration was created, denoted Spray A, where the influence of cross institution facilities and conditions was reported. This includes the influence of injectors, combustion vessels, and optical diagnostic tools. Hence, Spray A is a well-documented configuration and has been selected as the baseline case study.

4.1 ECN, Sandia Spray A Conditions

In this configuration, the experiment is carried out in a CVP vessel chamber facility at Sandia National Laboratories as shown in figure 1. The desired pressure and temperature conditions are achieved by spark igniting a premixed gas mixture to completion. The combustion products cool over a period of 700–2500 ms due to interaction with the vessel walls, with the chamber pressure decreasing slowly. Once the target conditions are detected, the fuel injector is triggered and the spray process begins.

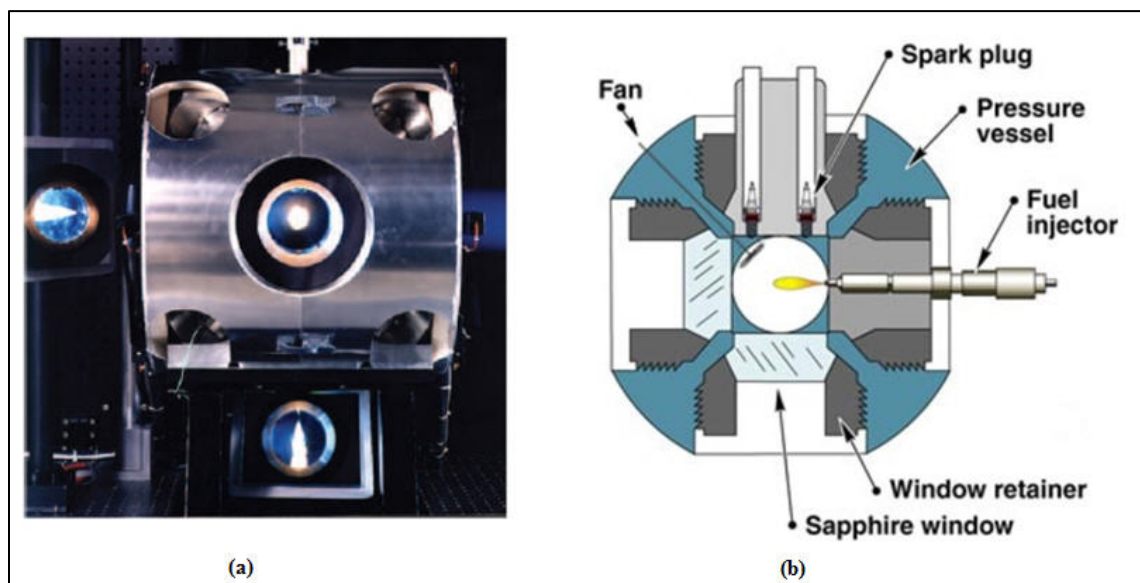


Figure 1. Sandia National Laboratories (a) CVP facility, (b) schematic of CVP setup.

The experimental facility also provides full optical access for line of sight or orthogonal optical diagnostics as seen in figure 1a. Figure 1b shows the setup with the positioning of the high-pressure common rail fuel injector, number of spark plugs, and fan location. To prevent wall impingement effects interfering during spray diagnostic process, the characteristic length of the vessel is typically designed to be 100 mm on each side. In order to prevent condensation of combustion products on the windows the vessel walls are heated electrically to engine surface temperatures. Multiple spark plugs are used to provide consistent ignition of a preburn lean mixture. Further details of the vessel geometry and diagnostics are presented in the review by Meijer et al. (16).

Spray A conditions are provided in table 1. The physical description corresponds to an evaporating fuel spray with 0% oxygen content (nonreacting), developing at diesel engine ambient conditions. A single hole, modern common rail injector with an injector diameter of 90 μ (Bosch CRIN 2.4) is used at typical diesel injection pressures. A single component diesel surrogate fuel (i.e., n-dodecane) is used due to its extensively well-characterized chemical and physical properties. Detailed and reduced mechanisms for n-dodecane are readily available from the literature (17).

Table 1. Injector and spray conditions (Spray A).

Sandia Conditions	Value	Sandia Conditions	Value
Fuel	n-dodecane	Injection Pressure (Mpa)	150
Ambient composition	0% Oxygen	Fuel Temperature (K)	363
Ambient temperature (K)	900	Nozzle Diameter (mm)	0.09
Ambient density (kg/m ³)	22.8	Injection Duration (ms)	1.5
Number of injector holes	1 (axial)	Injection mass (mg)	3.5

Numerical modeling with CONVERGE was conducted by using the multiphase Lagrangian particle tracking methods with wave-based spray submodels and the RANS methodology as described in section 3. There are several important procedures to be mindful of when running spray simulations. An Adaptive Mesh Refinement (AMR) procedure must be adopted to control the refinement levels in the vicinity of the spray. In this study, AMR is activated for the velocity field and its use is critical in keeping the cell counts at realistic operating levels.

Note also that fixed-grid embedding (in spray liquid core region) is used to define the reference minimum cell sizes, dx , and the embedding scale. The parameters are related through the base grid cell size, dx_{base} , as follows: $dx = dx_{base} \times 2/(embed\ scale^3)$. The coarsest base grid cell size of 2 mm and an embed scale of 3 corresponds to $dx = 0.25\ mm$.

When conducting grid refinements, a fixed number of injected particles will lead to an artificial increase of the liquid penetration length (9). This is due to the decrease of relative gas to liquid mass that occurs in each cell as the mesh is refined. Overlooking this can artificially cause the gas velocity to approach the particle velocity at every cell, decreasing particle drag. Table 2 documents the number of resolution levels, denoted as embedding scale, and the critical number of injected particles to achieve converged results. Note that to avoid going below a critical injected parcel number of 3000, the 1 mm and 2 injected parcel cases are identical.

Table 2. CFD embed scale and number of injected particles.

Embed Scale	dx (mm)	Injected Parcels
0	2	3125
1	1	3125
2	0.5	12,500
3	0.25	50,000
4	0.125	200,000
5	0.0625	800,000

Figure 2 shows the model convergent properties by inspection of the multiphase penetration profiles. Spatial grid-refinement studies were conducted using the grid and Lagrangian parcel parameters listed in table 2. In figure 2a, the liquid penetration diagnostic shows good agreement with the experimental data and convergent behavior. For the coarse case of $dx = 2\ mm$ and embed scale of zero, liquid penetration is over-predicted at peak by a factor of two. No

noticeable improvement is obtained with one additional level of grid refinement. However, the behavior drastically improves as the embedding scale elevates from a level of three to five, and finally converges to the experimental data. Figure 2b shows a similar trend with the vapor penetration length with the solution converging as the grid is refined. In this case, however, only convergence is obtained while the model solution at that refinement level shows discrepancies with the measured data. Figure 2c shows the convergence behavior of the peak liquid penetration with resolution level providing a guideline for grid criteria. It is important to note that due to the steady nature of the RANS turbulence model no cycle-to-cycle averaging was conducted and a single shot analysis is sufficient.

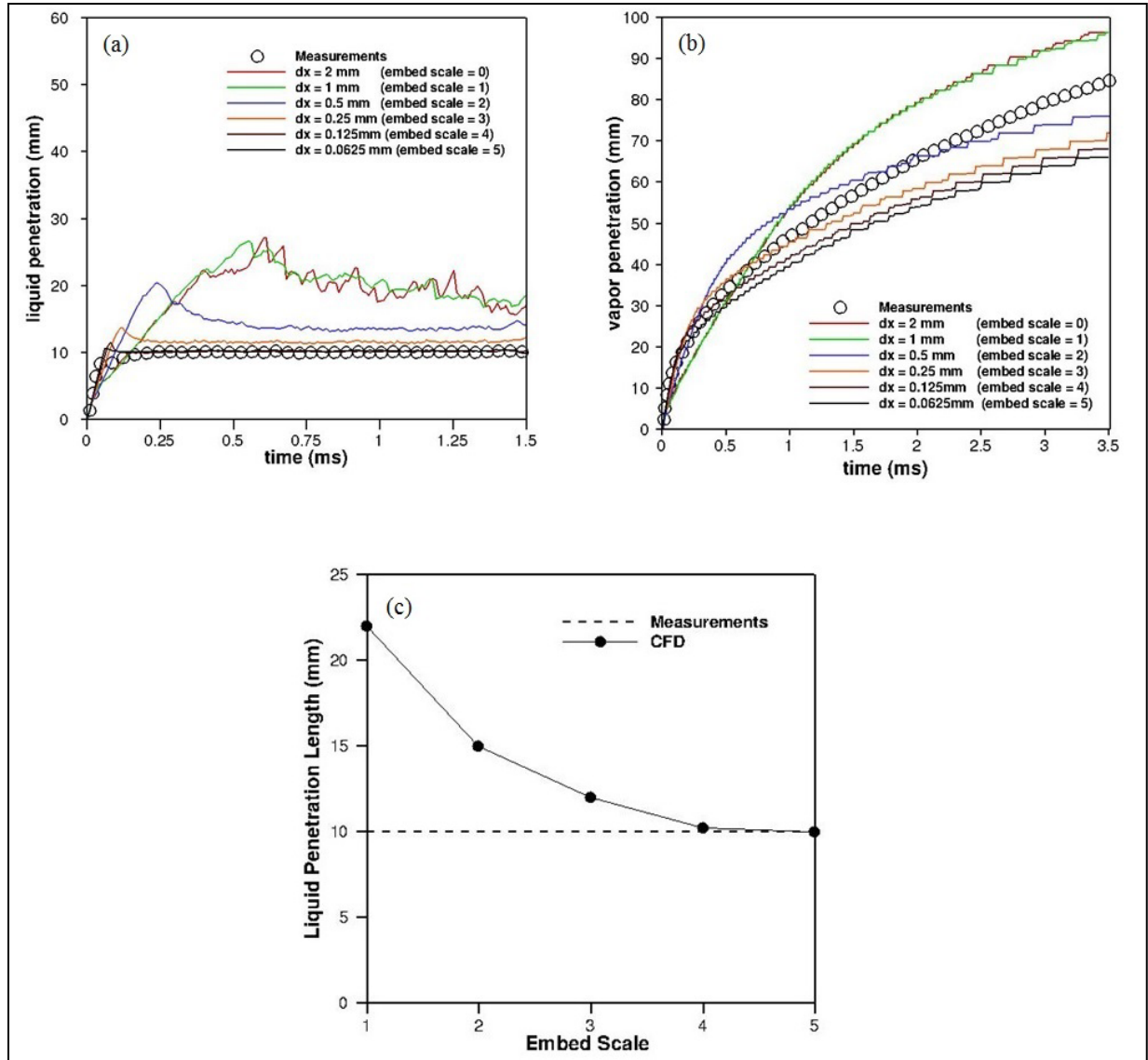


Figure 2. Spray A convergence properties at various embed scales corresponding to $dx = 2, 1, 0.5, 0.25, 0.125, 0.0625$ mm: (a) liquid penetration vs. time, (b) vapor penetration vs. time, (c) peak liquid penetration vs. embed scale.

In figure 3, an embedding scale of three was selected because it provided a good compromise between accuracy and computational cost. Also shown in figure 3 are multiphase penetration comparisons with Sandia, CMT-Motores (Spain), and IFP (France) measurements for additional reference (2). The liquid penetration profile in figure 3a shows two clearly marked regions. The regions are denoted by a transient region occurring up to a time of 0.25 ms and after this threshold a steady region. Note a penetration overshoot within the transient region of figure 3a. Although refining the grid does attenuate this over-shoot effect (see figure 2a), it does not eliminate it. This effect is thought to occur due to the present RANS turbulence treatment and its behavior with high-fidelity LES or DNS models and will be addressed in future works.

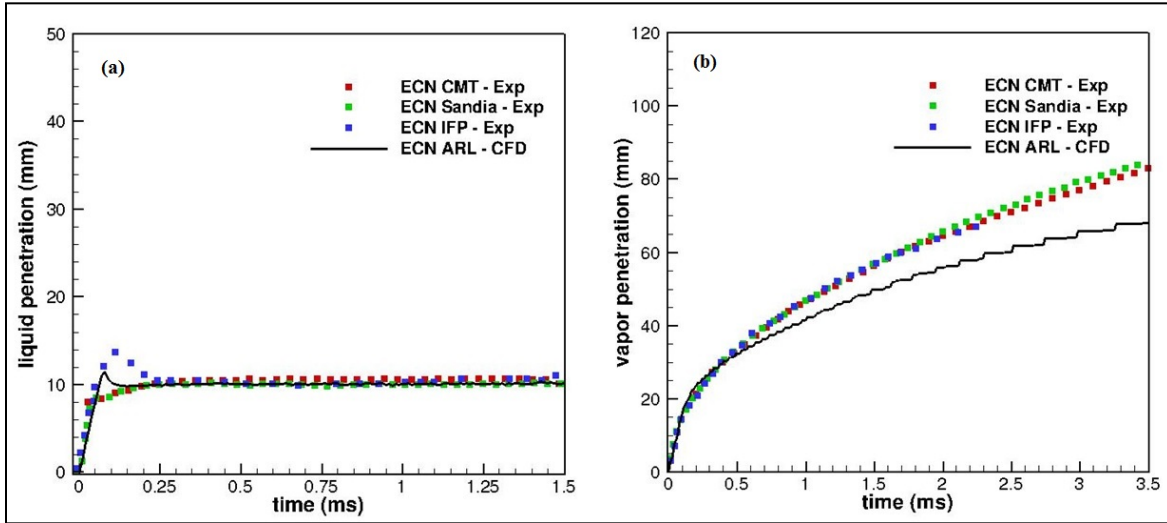


Figure 3. Multi-institutional experimental comparison of Spray A penetration profiles: (a) liquid penetration, (b) vapor penetration. Embed scale of three, $dx = 0.25$ mm.

Figure 3b shows the vapor penetration profile for Spray A at an embedding scale of three. It is noted that converged profile deviates from the experimental data, as was also the case in figure 2b. This effect has been observed previously by Senecal et al. (9) where he attributed this discrepancy to current uncertainties in measurement techniques. However the penetration velocity and rate of vapor penetration (slope of the profiles) is in close agreement.

Figure 4 shows comparison with the experimental images reported by Pickett et al. (2) for the same conditions. The measurements were obtained using Mie scatter optical diagnostics and the images are time averaged. Note that the reporting discrepancies with the IFP data (peak in penetration profile) has been reported and thought to be due to differences in laser optical diagnostic methodologies (orientation of laser light).

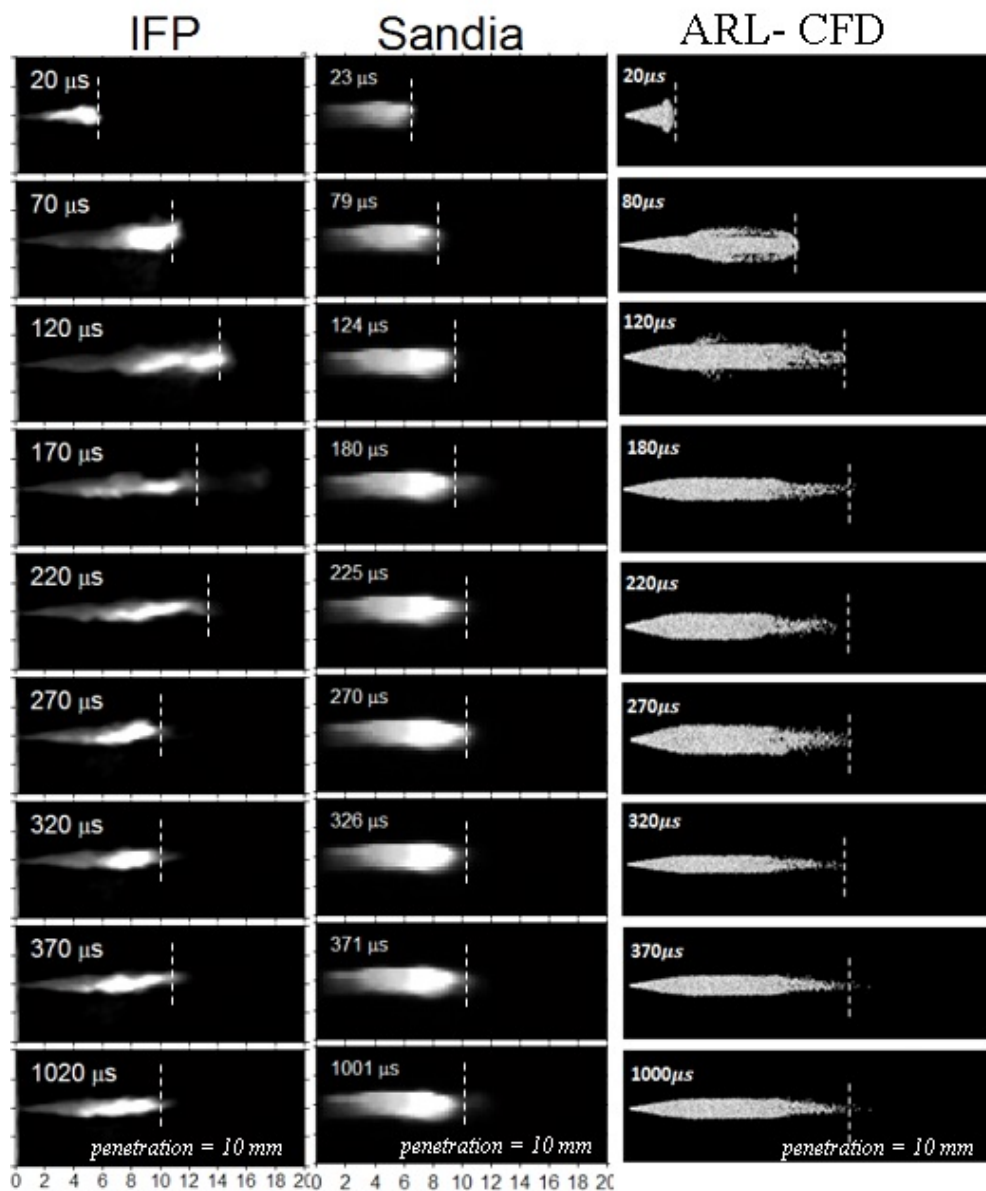


Figure 4. Mie scattering imaging sequence at IFP and Sandia and comparison to ARL's CFD model for Spray A conditions.

Figure 5a and 5b show the Eulerian gas phase velocity and fuel-mass fraction (n-dodecane) contour variations surrounded by the vapor mass fraction line, $Y_f = 0.01$. Also shown are the Lagrangian liquid phase particles convecting downstream subject to a uniform heating load and shear forces. Note that peak values will originate from the nozzle orifice rapidly decreasing in magnitude due to mixing process with the stagnant environment. Time intervals corresponding to 0.5, 1.0, and 1.5 ms are selected to show the spray process.

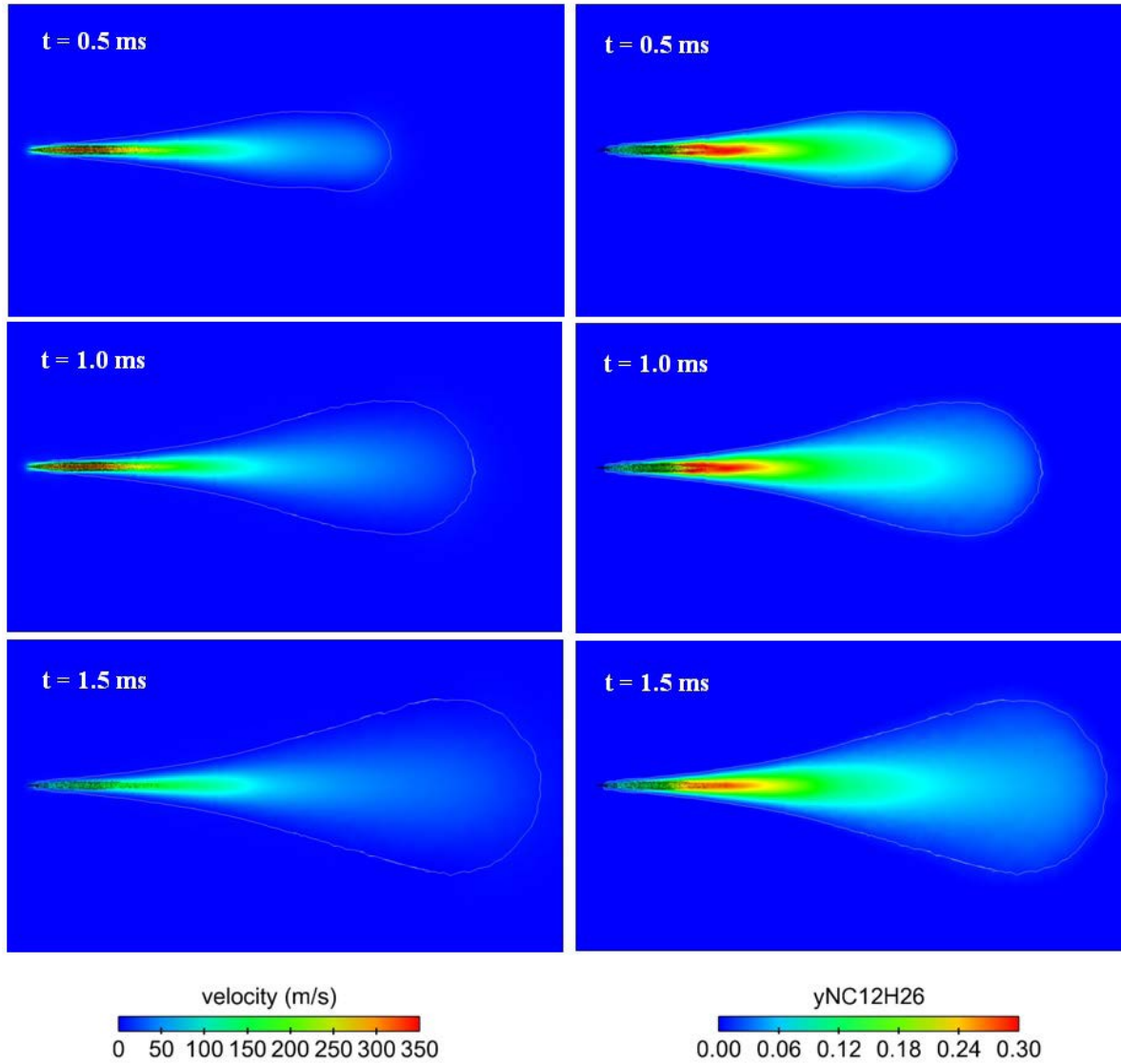


Figure 5. Spray A visualization (a) contour of velocity and (b) contours of fuel-mass fraction. Note that spray is surrounded by the vapor line at $Y_f = 0.01$.

4.2 ECN, CMT Spray A conditions (Fuel-Temperature Effects)

In this configuration, the experiment is carried out in a CPF test chamber that has the capability to reach peak conditions of 1000 K and 15 MPa, figure 6a. It does not require a pre-burn phase to obtain this condition and rather it is comprised of four subsystems (1) gas compressor, (2) gas heater, (3) test vessel, and (4) control system to achieve nearly quiescent and a steady thermodynamic conditions. A gas initially stored in a high-pressure reservoir, flows continuously through the vessel via volumetric compressors. Electrical heaters are used to increase the temperature of the flowing gas up to the selected temperature. A control system (closed loop proportional-integral-derivative [PID] controller) adjusts for both the chamber pressure and the power of the heater to obtain uniform conditions for the test. To minimize temperature inhomogeneity in the testing region the thinner inner walls are covered with an insulating layer and have the function of reducing the heating of the outer shell. Note the initial conditions differ from Sandia's combustion vessel, since there are no combustion products present.

Figure 6b shows the optical setup used for Mie scattering technique with frontal illumination. The spray region is illuminated with a continuous Xenon-arc lamp where the scattered light is recorded by way of a high-speed CMOS camera (Photoron Fastcam).

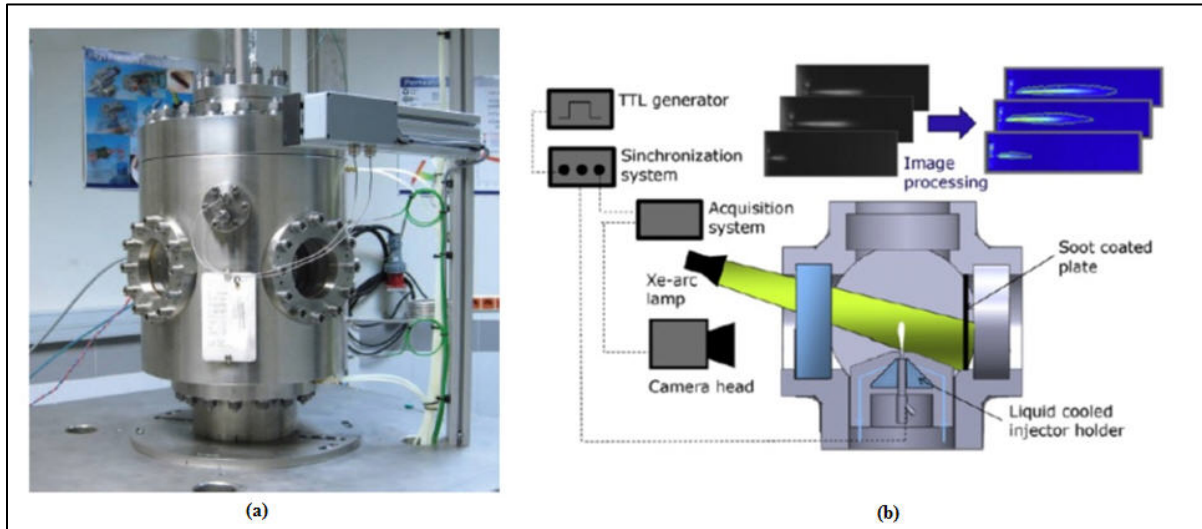


Figure 6. CMT-Motores, Universidad Politecnica de Valencia: (a) CPF facility, (b) schematic of CPF setup.

Baseline Spray A conditions, as provided in table 1, are also invoked in this study. It is important to note the difference in setup between the two studies. In the present study, there is a strong emphasis on characterizing fuel-temperature effects, and as such, fuel-coolant temperatures are varied accordingly. In addition, the vessel gas temperature is allowed to vary from 820 to 900 K, as well as the injection pressure from 50, 100, to 150 MPa. Vessel conditions are given in table 3.

Table 3. CMT vessel conditions.

CMT Conditions	Value	CMT Conditions	Value
Fuel	n-dodecane	Injection pressure (Mpa)	50, 100, 150
Ambient composition	100% N_2	Fuel temperature (K)	363
Ambient temperature (K)	820, 900	Nozzle diameter (mm)	0.09
Ambient density (kg/m^3)	22.8	Injection duration (ms)	4.5
Number of injector holes	1 (axial)	Injection mass (mg)	3.5

Note that there is a strong distinction from the fuel-coolant temperature and the real fuel temperature. The relationship between fuel coolant and real temperature has been studied through the use of a dummy injector test rig. Because there is no fluid flow through the dummy injector the outer nozzle hole has been shut, while the injector needle contains an axially drilled hole with the upstream part to insert a thin thermocouple. Temperature readings are made axially up to 33-mm upstream from the injector sac to provide temperature readings in this region and study the relationship between both lines. For further reference on the dummy injector set up and instrumentation, see Payri et al. (3).

Table 4 presents the measured fuel temperature at the injector sac volume (T_f) for two vessel ambient conditions, $T_{amb} = 820$ and 900 K. Three coolant conditions (T_c) were tested for each vessel condition and the sac fuel temperature was determined through a sliding thermocouple instrumentation. In this study, the sac fuel temperature, T_f , has been used as the best approximation to the CFD model fuel-temperature boundary condition.

Table 4. Coolant and injector sac fuel temperature.

$T_{amb} (K)$	$T_{amb} (K)$	$T_c(K)$	$T_{amb} (K)$	$T_{amb} (K)$	$T_c(K)$
820	293	331	900	293	341
820	318	358	900	318	369
820	343	377	900	343	391

Table 5 is the test matrix; it presents a total of nine (9) case studies that have been selected for validation purposes in this report. Cases A1–A3 correspond to constant high-pressure fuel injection at the standard Spray A conditions while varying fuel temperature. Cases B1–B3 is a collection of intermediate-to-low vessel temperature condition at $T_{amb} = 820$ K studied while varying the injection pressure. Together with cases B4–B6 they also quantify the effect of variations in fuel temperature at various conditions.

Table 5. CONVERGE test cases.

Case	Injection Conditions	Vessel Conditions
CMT-A1	$T_f = 341K; P_{inj} = 1500 \text{ bar},$	$P_\infty = 60 \text{ bar}; T_\infty = 900K,$ $\rho_\infty = 22.8 \text{ kg/m}^3$
CMT-A2	$T_f = 369K; P_{inj} = 1500 \text{ bar}$	
CMT-A3	$T_f = 391K; P_{inj} = 1500 \text{ bar}$	
Case	Injection Conditions	Vessel Conditions
CMT-B1	$P_{inj} = 500 \text{ bar}; T_f = 331 \text{ K}$	$P_\infty = 60 \text{ bar}; T_\infty = 820K,$ $\rho_\infty = 22.8 \text{ kg/m}^3$
CMT-B2	$P_{inj} = 1000 \text{ bar}; T_f = 331 \text{ K}$	
CMT-B3	$P_{inj} = 1500 \text{ bar}; T_f = 331 \text{ K}$	
Case	Injection Conditions	Vessel Conditions
CMT-B4	$P_{inj} = 500 \text{ bar}; T_f = 377 \text{ K},$	$P_\infty = 60 \text{ bar}; T_\infty = 820K,$ $\rho_\infty = 22.8 \text{ kg/m}^3$
CMT-B5	$P_{inj} = 1000 \text{ bar}; T_f = 377 \text{ K},$	
CMT-B6	$P_{inj} = 1500 \text{ bar}; T_f = 377 \text{ K},$	

A rate-of-injection boundary condition for the simulations was specified through the use of hydro-dynamic fuel-mass flow-rate application. This application was developed by researchers of CMT-Motores (Spain) in an effort to understand the actual rate of injection during very fast injector opening transients. It is an online virtual flow-rate generator that considers various injector operating conditions; it is readily available at <http://www.cmt.upv.es/ECN03.aspx>. This tool was applied to generate the necessary rate of injections as shown in figure 7.

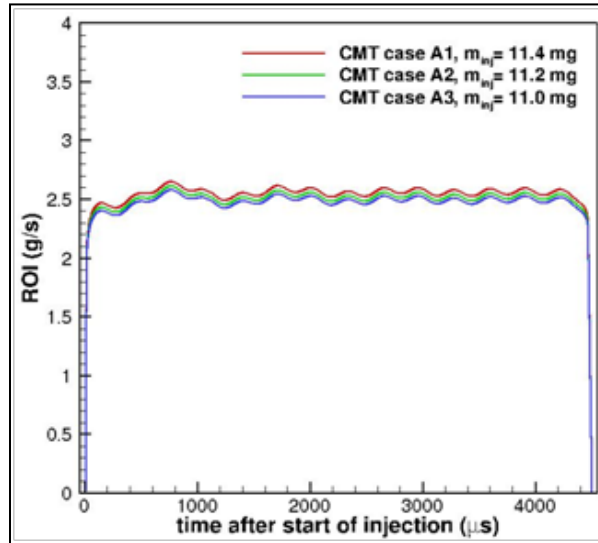


Figure 7. Rate of injection (ROI) profiles for CMT cases A1–A3 using the CMT virtual injection generator.

Figure 8a shows that the modeled fuel-temperature effects are not as pronounced as the experimental case. In measurements, we see about 1-mm decrease in liquid penetration length when temperature is increased from 341, 369, to 391 K. Simulations capture this trend but with at a reduced magnitude of 0.5-mm per case. The effect on the vapor penetration is negligible as seen in figure 8b. There were no available measurements for comparison of figure 8b; hence, modeled results are presented alone.

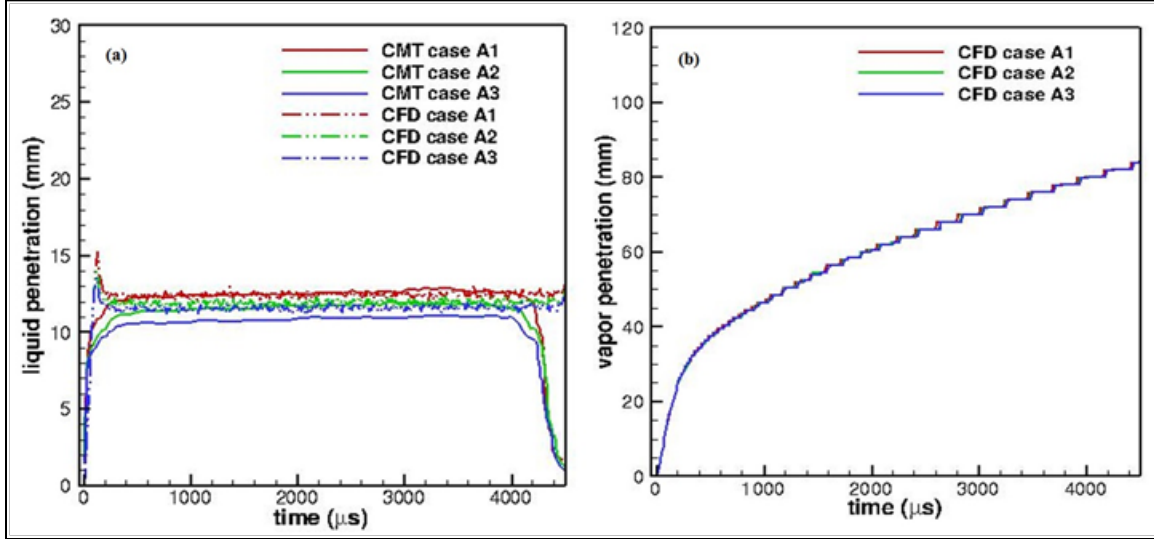


Figure 8. Spray penetration profiles at $P_{\infty} = 60 \text{ bar}$; $T_{\infty} = 900\text{K}$, $\rho_{\infty} = 22.8 \text{ kg/m}^3$ ambient conditions with fixed $P_{inj} = 1500 \text{ bar}$ while varying fuel temperature $T_f = 341\text{K}, 369\text{K}, 391\text{K}$.

Figures 9 and 10 show the liquid phase penetration response to various operating conditions at a fixed vessel temperature of $T_{amb} = 820 \text{ K}$. It is important to note that this condition represents the low-temperature regime of diesel engine conditions and it represents a departure from the standard Spray A conditions. Temperature variations in the injector and vessel conditions will impact the fuel's physical properties while imposing different heating loads. Higher heating loads and fuel temperatures will result in shorter steady state liquid penetration lengths. Traditionally it has been challenging for multiphase CFD solver to capture low-temperature behavior accurately and hence a validation study in this regime is important.

Figure 9a is the rate of injection profile for each injection pressure obtained using the CMT virtual injector generator for cases CMT B1–B3. The total injected mass was obtained through integration of each profile using a simple MATLAB script. Figure 9b–9d shows the impact of the injector pressure on the fuel-penetration behavior. As it is expected higher rail pressure increases the rate of atomization leading to modest decreases in liquid lengths. Note that the vapor penetration length increases with rail pressure, because it is also dependent on the atomization behavior. In figure 10 the same behavior is studied but with a higher fuel-temperature condition, cases CMT B4–B6. Figure 10a, shows the rate of injection profiles, while figure 10b–10d shows the liquid and vapor penetration behaviors with pressure at this condition. Because of the steady

state modeling technique (RANS turbulence model) no profile averaging was necessary, and a single shot study was sufficient. Note also that due to the longer simulation time, $4.5 \mu\text{s}$ versus $1.5 \mu\text{s}$ for Sandia Spray-A case, a larger number of particles were injected to avoid spurious oscillations in the profiles. A simple study determined that one million total injected particles were sufficient to account for evaporation and the longer injection process. Also, the computational grid was prescribed based on the resolution studies for Spray A. This was determined using a base grid cell size, $dx_{base} = 2 \text{ mm}$, and an embedding scale level of three, as follows: $dx = dx_{base} \times 1/(dx_{base}^{escale_level})$. Hence the minimum grid cell size at the present embed scale corresponds to $dx = 0.25 \text{ mm}$.

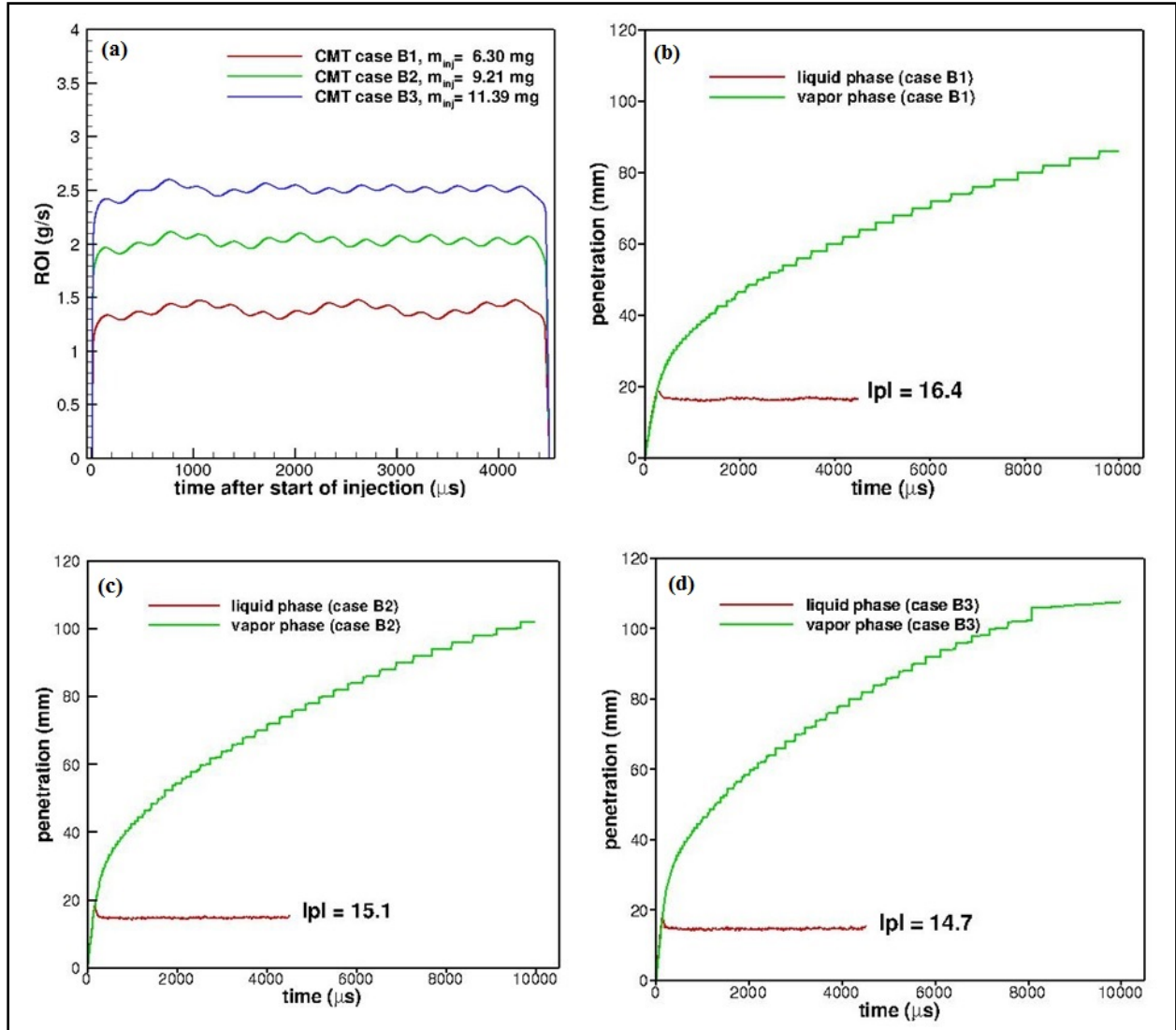


Figure 9. Spray injection and penetration profiles at $P_{\infty} = 60 \text{ bar}$; $T_{\infty} = 820 \text{ K}$; $\rho_{\infty} = 22.8 \text{ kg/m}^3$ ambient conditions and fuel temperature $T_f = 331 \text{ K}$. (a) ROI profiles used for cases b–d, (b) liquid/vapor profiles at $P_{inj} = 500 \text{ bar}$, (c) liquid/vapor profiles at $P_{inj} = 1000 \text{ bar}$, liquid/vapor profiles at $P_{inj} = 1500 \text{ bar}$.

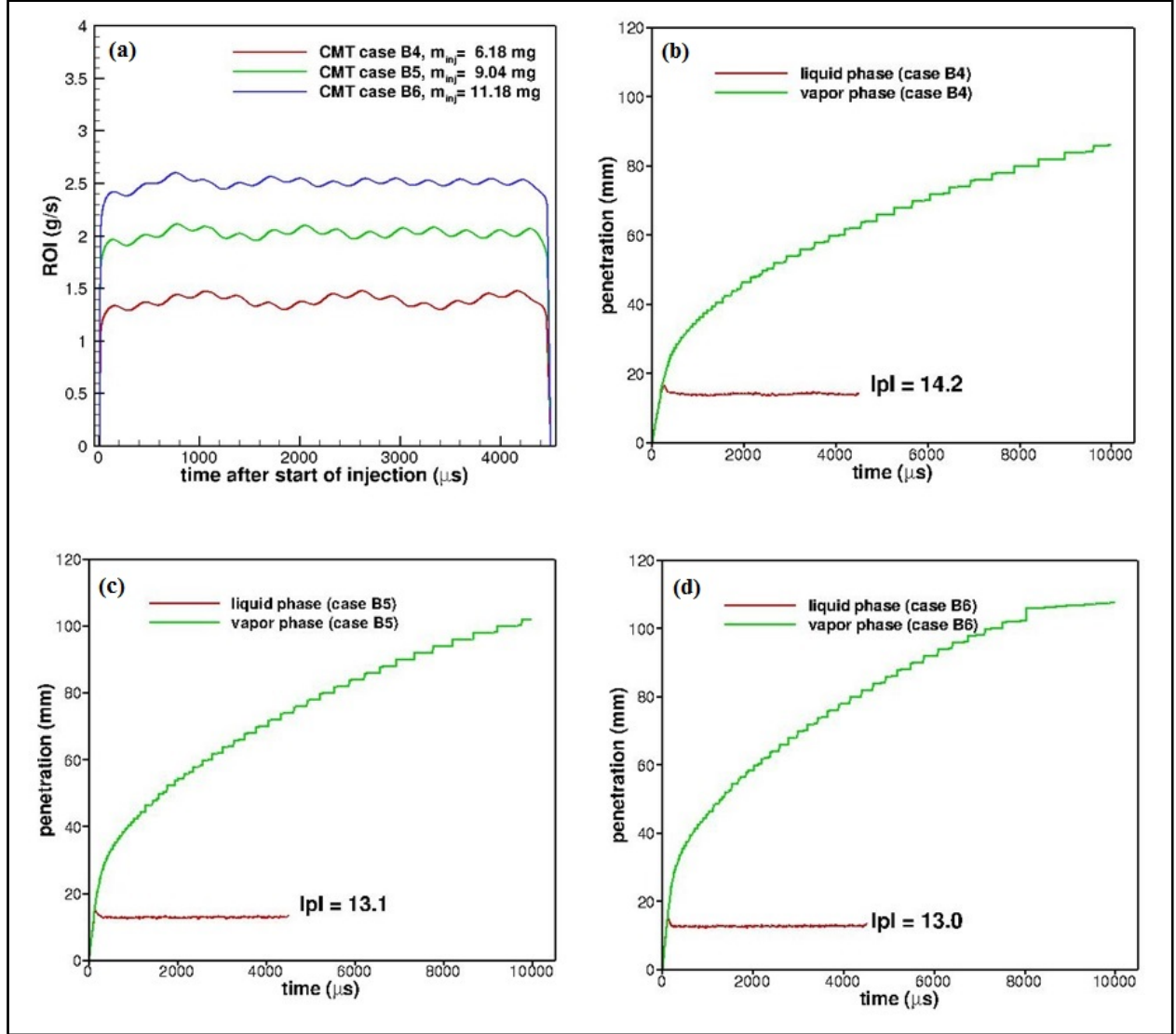


Figure 10. Spray injection and penetration profiles at $P_{\infty} = 60$ bar; $T_{\infty} = 820$ K, $\rho_{\infty} = 22.8$ kg/m³ ambient conditions and fuel temperature $T_f = 377$ K. (a) ROI profiles used for cases b–d, (b) liquid/vapor profiles at $P_{inj} = 500$ bar, (c) liquid/vapor profiles at $P_{inj} = 1000$ bar, liquid/vapor profiles at $P_{inj} = 1500$ bar.

In order to enable comparison with current simulations, steady state results are presented in figure 11a–11b for cases CMT B1–B6. An averaged liquid penetration length was calculated in the steady state region from 3.0 to 4.0 μs; the same approach was used with simulation results. Figure 11a–11b depicts the liquid length variations with pressure at $T_f = 331$ K, 377 K, respectively. The effect of fuel temperature on the penetration length is clearly observed at each pressure interval. Note that the profiles retain their behavior while reducing almost uniformly in magnitude. At fixed fuel-temperature conditions, the largest impact on penetration length is consistently seen when increasing the injection pressure from 500 to 1000 bar. Model comparison to experiments show good agreements at each pressure interval for both fuel-

temperature conditions. The small discrepancies between experiments and simulations may arise due to fuel-temperature calibration effects. It is also important to note that in experiments the most accurate temperature conditions was probed at the injector sac volume as was explained earlier. This temperature location reading is different to what is specified at the CFD boundary condition, which corresponds to the fuel temperature at the tip of the nozzle (downstream of the sac volume). This discrepancy in specification is subtle but shows the need for better consistency between measurements and experiments in order to avoid calibration or tuning of CFD models.

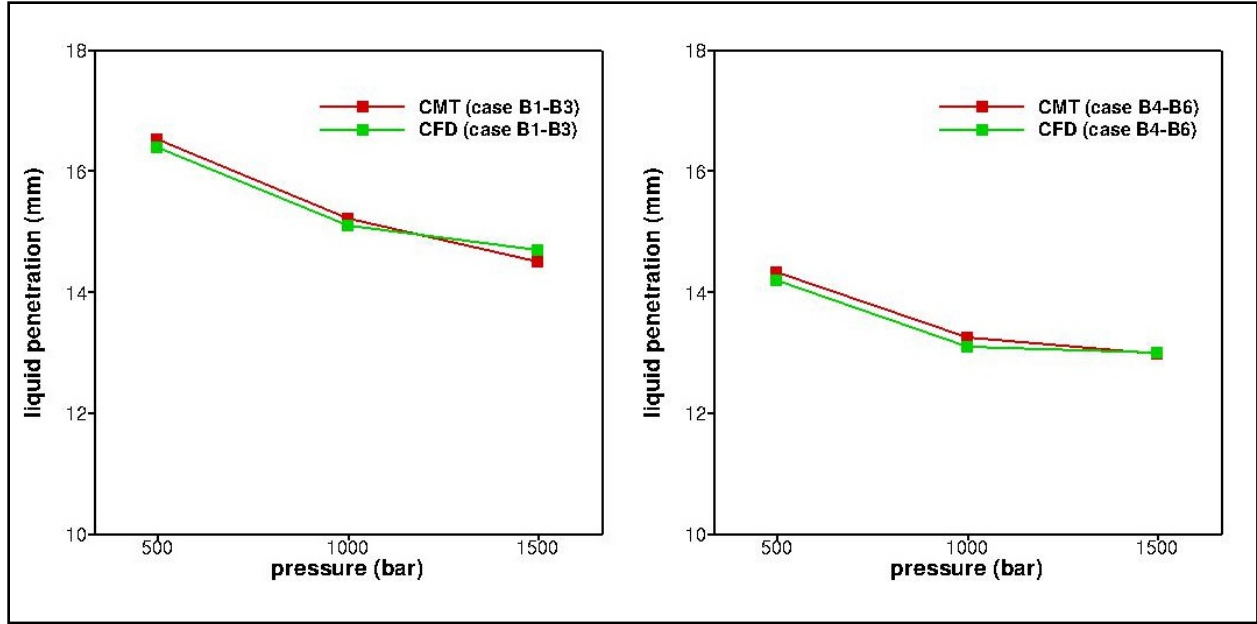


Figure 11. Effect of T_f variation over liquid penetration length for different injection pressures (at $\rho_\infty = 22.8 \text{ kg/m}^3$) for (a) $T_f = 331 \text{ K}$, (b) $T_f = 377 \text{ K}$.

5. Conclusions

The studies conducted as a part of this report presents successful validations for nonreacting spray simulations under typical diesel engine conditions. Validation with Sandia's Spray-A unique operating condition was targeted to demonstrate the grid-convergence properties (9). Note that AMRs and grid-embedding techniques were used in obtaining numerical convergence. Grid-convergence studies were useful in determining an adequate grid resolution while maintaining model accuracy. Subsequent validation studies with the CMT-Motores database were also targeted to explore the fuel-temperature effect on spray parameters (3). This study was conducted at a lower vessel temperature condition and represents a departure from Spray A conditions. The effect of fuel temperature was seen to influence mainly the liquid penetration length and to be less pronounced for the vapor penetration profiles. Also, the numerical results show good agreement with measurements. The reported discrepancies are currently thought to be

due to providing nominal fuel-temperature boundary condition in the CFD model and the “actual” fuel temperature in the experiment. This finding raises the need for better consistency between measurements and experiments in order to avoid calibration or tuning of CFD models.

The results presented in this briefing provide a benchmarked model able to predict engine spray at various challenging diesel operating conditions of interest to the Army. Future efforts will be aimed at conducting an extended range of benchmark studies with JP-8 surrogate fuels including detailed studies of mixture formation process, soot formation and oxidation, including split injection strategies.

6. References

1. Siebers, D. Liquid-Phase Fuel Penetration in Diesel Sprays, *SAE paper 980809*, 1998.
2. Pickett, L.; Genzale, C.; Bruneaux, G. Comparison of Diesel Spray Combustion in Different High-Temperature, High-Pressure Facilities, *SAE International*, 10FFL-0315, 2010.
3. Payri, R.; García-Oliver, J. M.; Bardi, M.; Manin, J. Fuel Temperature Influence on Diesel Sprays in Inert and Reacting Conditions. *Applied Thermal Engineering* **2012**, 35, 185–195.
4. Wang, Y. J.; Im, K.-S.; Fezzaa, K.; Lee, W. K.; Wang, J.; Micheli, P.; Laub, C. Quantitative X-Ray Phase-Contrast Imaging of Air-Assisted Water Sprays With High Weber Numbers. *Applied Physics Letters* October **2006**, 89 (15), 151913.
5. Meyer, T. R.; Schmidt, J. B.; Nelson, S. M.; Drake, J. B. Janvrin, D. M.; Heindel, T. J. Three-Dimensional Spray Visualization Using X-ray Computed Tomography, in *ILASS Americas, 21st Annual conference on Liquid Atomization and Spray Systems*, Orlando, FL, 2008.
6. Coletti, F.; Benson, M. J.; Sagues, A. L.; Miller, B. H.; Fahrig, R.; Eaton, J. K. Three-Dimensional Mass Fraction Distribution of a Spray Measured by X-Ray Computed Tomography. *ASME Journal of Engineering for Gas Turbines and Power*, 2013.
7. Banerjee, S.; Rutland, C. On LES Grid Criteria for Spray Induced Turbulence. *SAE International Paper 2012-01-0141*, 2012.
8. Bharadwaj, N. Rutland, C. J.; Chang, S. Large Eddy Simulation Modelling of Spray-Induced Turbulence Effects. *International Journal of Engine Research* **2009**, 10 (2) 97–119.
9. Senecal, P.; Pomraning, E.; Richards, K.; Som, S. Grid-Convergent Spray Models for Internal Combustion Engine CFD Simulations, in *Proceedings of the ASME 2012 Internal Combustion Engine Division Fall Technical Conference (ICEF2012-92043)*, 2012.
10. Som, S.; Aggarwal, S.; Effects of Primary Breakup Modeling on Spray and Combustion Characteristics of Compression Ignition Engines. *Combustion and Flame* (157), 2010, 1179–1193.
11. Senecal, P.; Pomraning, E.; Xue, Q.; Som, S. Large Eddy Simulation of Vaporizing Sprays Considering Multi-Injection Averaging and Grid-Convergent Mesh Resolution. *Proceedings of the ASME 2013 Internal Combustion Engine Division Fall Technical Conference (ICEF2013-19082)*, 2013.

12. Xue, Q.; Som, S.; Senecal, P. K.; Pomraning, E. A Study of Grid Resolution and SGS Models for LES Under Non-reacting Spray Conditions. *ILASS Americas, 25th Annual Conference on Liquid Atomization and Spray Systems*, Pittsburgh, PA, May 2013.
13. Issa, R. Solution of the Implicitly Discretised Fluid Flow Equations By Operator-Splitting. *Journal of Computational Physics* **January 1986**, 62 (1), 40–65.
14. Reitz, R.; Diwakar, R. Effect of Drop Breakup on Fuel Sprays, SAE Technical Paper 860469, 1986.
15. Bravo, L.; Kweon, C. Review of Liquid Fuel Atomization Models for 3D-CFD Analysis. *ARL-Report T14-134-S*; 2013.
16. Meijer, M.; Somers, B.; Johnson, J.; Naber, J.; Lee, S.; Malber, L.M.; Bruneaux, G.; Pickett, L.M.; Bardi, M.; Payri, R.; Bazyn, T. Engine Combustion Network (ECN): Characterization and Comparison of Boundary Conditions for Different Combustion Vessels. *Atomization and Sprays* **2012**, 22 (9), 777–806.
17. Pitz, W.; Westbrook, C.K.; Herbinet, O.; Silke, E.J. Progress in Chemical Kinetic Modeling for Surrogate Fuels (LLNL-CONF-404514). In *the 7th COMODIA International Conference on Modeling and Diagnostics for Advanced Engine Systems*, 2008.

List of Symbols, Abbreviations, and Acronyms

AMR	Adaptive Mesh Refinement
ANL	Argonne National Laboratory
ARL	U.S. Army Research Laboratory
CFD	Computational Fluid Dynamics
CPF	Constant Pressure Flow
CSI	Convergent Science, Inc.
CT	computed tomography
CVP	Constant Volume Preburn
DNS	direct numerical simulation
ECN	Engine Combustion Network
HEUI	Hydraulically-actuated Electronically-controlled Unit Injector
HRJ	Hydrotreated Renewable Jet
IPK	Iso-Paraffinic Koresene
KH	Kelvin-Helmholtz
KH-ACT	Kelvin-Helmholtz-Aerodynamics Cavitation Turbulence
LES	large-eddy simulation
MPI	Message Passing Interface
PID	proportional-integral-derivative
PISO	Pressure Implicit with Splitting of Operator
RANS	Reynolds-averaged Navier-Stokes
ROI	rate of injection
RT	Rayleigh-Taylor
UAV	unmanned aerial vehicle
VTD	Vehicle Technology Directorate

1 DEFENSE TECHNICAL
(PDF) INFORMATION CTR
DTIC OCA

2 DIRECTOR
(PDF) US ARMY RESEARCH LAB
RDRL CIO LL
IMAL HRA MAIL & RECORDS MGMT

1 GOVT PRINTG OFC
(PDF) A MALHOTRA

1 DIR USARL
(PDF) RDRL VTP
L BRAVO